MATERIALS SCIENCE

Nanoscale mapping of chemical composition in organic-inorganic hybrid perovskite films

R. Szostak[1,2], J. C. Silva[1], S.-H. Turren-Cruz[3,4], M. M. Soares[2], R. O. Freitas[2], A. Hagfeldt[4], H. C. N. Tolentino[2]*, A. F. Nogueira[1]*

Lead-based organic-inorganic hybrid perovskite (OIHP) solar cells can attain efficiencies over 20%. However, the impact of ion mobility and/or organic depletion, structural changes, and segregation under operating conditions urge for decisive and more accurate investigations. Hence, the development of analytical tools for accessing the grain-to-grain OIHP chemistry is of great relevance. Here, we used synchrotron infrared nanospectroscopy (nano-FTIR) to map individual nanograins in OIHP films. Our results reveal a spatial heterogeneity of the vibrational activity associated to the nanoscale chemical diversity of isolated grains. It was possible to map the chemistry of individual grains in CsFAMA [$Cs_{0.05}FA_{0.79}MA_{0.16}Pb(I_{0.83}Br_{0.17})_3$] and FAMA [$FA_{0.83}MA_{0.17}Pb(I_{0.83}Br_{0.17})_3$] films, with information on their local composition. Nanograins with stronger nano-FTIR activity in CsFAMA and FAMA films can be assigned to PbI_2 and hexagonal polytype phases, respectively. The analysis herein can be extended to any OIHP films where organic cation depletion/accumulation can be used as a chemical label to study composition.

INTRODUCTION

Organic-inorganic hybrid perovskite (OIHP) materials have markedly changed the photovoltaic scenario with power conversion efficiencies over 20% (*1*) in only 6 years. Despite this rapid development, stability issues related to ion mobility and/or organic depletion, structural changes, and segregation under operating and illumination conditions still hinder their real-world scale application. At room temperature, the presence of moisture (>50% relative humidity) leads to an irreversible degradation of the perovskite, where the main product is lead iodide (and lead bromide in mixed halide perovskites) (*2*). Degradation has a direct impact on the power conversion efficiency of OIHP solar cells (*3*). Despite degradation mechanisms being normally expressed as a bulk property, they are more likely to take place in the scale of single grains and between the boundaries.

The recent advances in efficiency attained by compositional engineering have enabled devices to operate with improved stability (*4*, *5*). However, the question on how the different structural phases are distributed in the structure, influencing the structural-optical properties and device's performance, is still open. A limited number of reports have been dedicated to map the nanoscale composition in perovskite samples, especially where different organic and inorganic cations and/or mixed halides are present. Hence, the development of analytical tools for accessing the grain-to-grain chemistry of OIHP is of paramount importance. Cacovich *et al.* (*6*) used energy-dispersive x-ray spectroscopy in a scanning transmission electron microscope to map the degradation through the cross section of perovskite films, highlighting the migration of elements in an aged solar cell device. A similar study was carried out by Christians *et al.* (*7*) using time-of-flight–secondary ion mass spectrometry. Segregation of iodide and bromide in mixed cation/mixed halide perovskite was demonstrated by Nazeeruddin and co-workers using a high-resolution helium ion microscope coupled to a secondary ion mass spectrometer (*8*) and

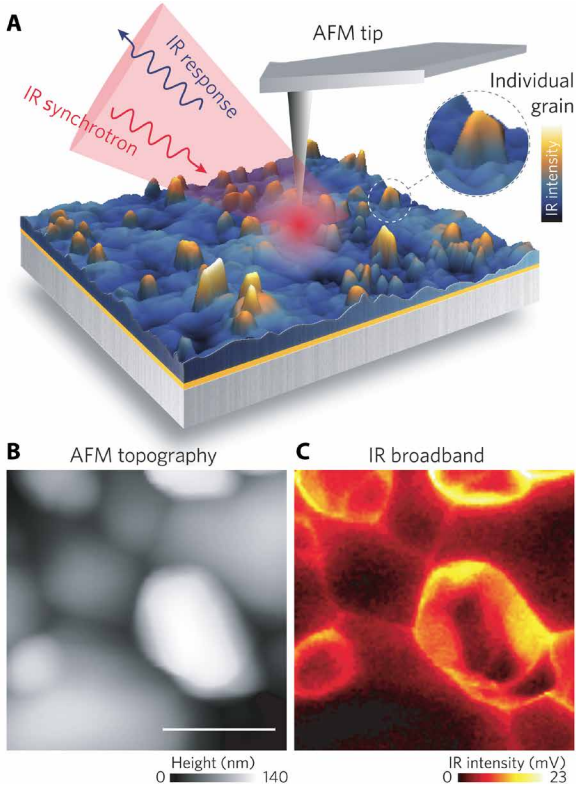

Fig. 1. Nano-FTIR analysis of OIHP films. (**A**) Synchrotron broadband IR radiation is focused onto a metallic tip that tightly confines the fields at its apex for further interaction with the sample surface in standard tapping-mode AFM. AFM mapping retrieves nanoscale morphology (**B**) and IR broadband intensity (**C**) of individual grains in the ~150-nm-thick OIHP film. The IR broadband image (C) reveals changes in the vibrational response of specific OIHP grain boundaries that are further associated to early stages of organic depletion in the film. Scale bar, 200 nm.

[1]University of Campinas (UNICAMP), Laboratório de Nanotecnologia e Energia Solar, Chemistry Institute, Campinas, PO Box 6154, 13083-970, Brazil. [2]Brazilian Synchrotron Light Laboratory (LNLS), Brazilian Center for Research in Energy and Materials (CNPEM), Campinas, SP 13083-970, Brazil. [3]Helmholtz-Zentrum Berlin für Materialien und Energie, Kekuléstraße 5, 12489 Berlin, Germany. [4]Laboratory of Photomolecular Science, Institute of Chemical Sciences and Engineering, École Polytechnique Fédérale de Lausanne, 1015, Lausanne, Switzerland.
*Corresponding author. Email: anafla@unicamp.br (A.F.N.); helio.tolentino@lnls.br (H.C.N.T.)

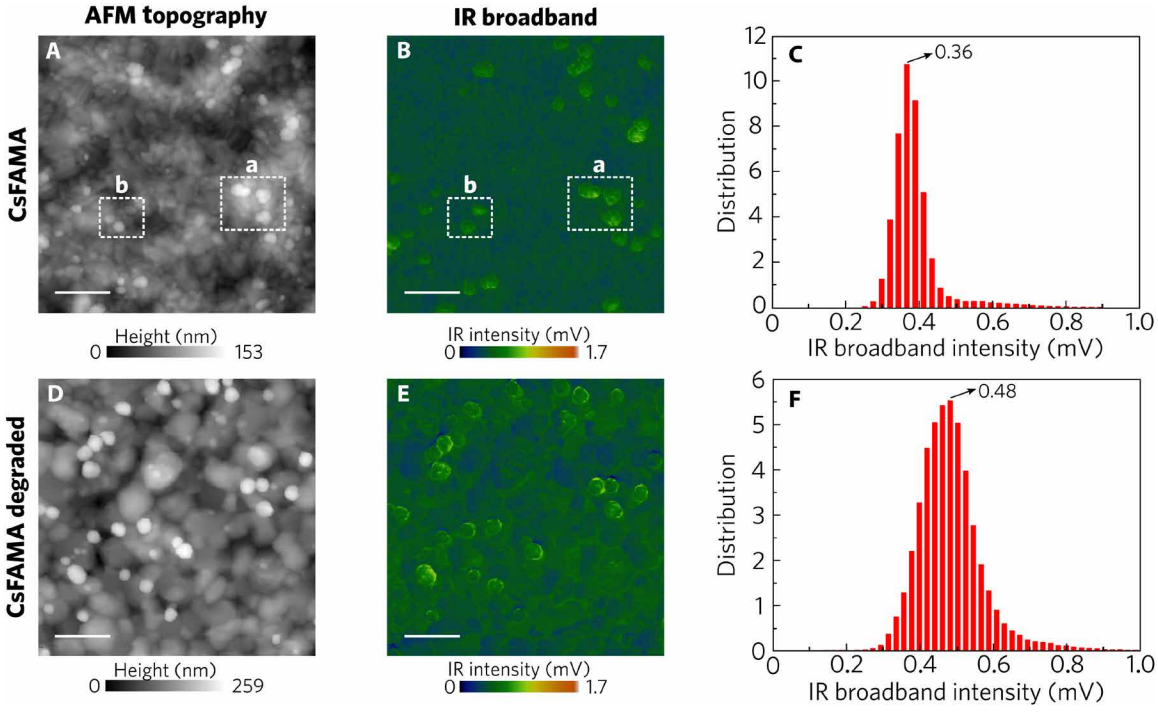

Fig. 2. Topography and IR broadband imaging of the perovskites. Topography images (5 μm by 5 μm) of (**A**) CsFAMA and (**D**) CsFAMA degraded samples. The topography of the CsFAMA sample shows an even background layer with grains ranging from few to several hundreds of nanometers. The IR broadband image revealed an inhomogeneity in vibrational activity. Particles with stronger activity are associated with higher height observed in the region highlighted by the white dashed square a in (A) and (**B**), but nanoparticles with stronger activity not associated with higher height in the topography image as highlighted in square b are also observed. The induced degradation led to a growth of the grains, and the vibrational activity became more intense (**E**). From the IR broadband intensity histograms, there is a shift in the intensity from 0.36 mV in the CsFAMA sample (**C**) to 0.48 mV in the CsFAMA degraded sample (**F**). Scale bars, 1 μm.

secondary electron hyperspectral imaging (*9*). On the basis of synchrotron radiation, nanoscale x-ray diffraction (XRD) and fluorescence were used to map structural and elemental properties of perovskites (*10*, *11*). Despite that, elemental sensitivity and sample requirements prevent electron microscopy to access local chemical composition of perovskite films in cell operation conditions. On the other hand, established techniques such as Raman and Fourier transform infrared (FTIR) spectroscopy are nondestructive and label-free tools for chemical analysis of materials, but with spatial resolution limited by diffraction (~λ/2). Alternatively, a variety of techniques combines atomic force microscopy (AFM) with IR microscopy to achieve subdiffraction resolution in the chemical analysis (*12*–*14*). Recently, photothermal induced resonance microscopy was applied on the study of a variety of perovskite films regarding methylammonium (MA) migration driven by an external bias (*15*), thermal annealing effects (*16*), local distribution of Cl^- and I^- (*17*), and ferroelastic domains (*18*). The correlated peak force IR microscopy has been used to map inhomogeneity in $CH_3NH_3PbBr_3$ (*13*).

Scattering scanning near-field optical microscopy (s-SNOM) is a unique technique able to unveil broadband complex optical response of materials with spatial resolution better than 25 nm (*19*, *20*). In s-SNOM, free-space radiation (incident IR beam broad radiation) is closely confined at the apex of a metallic AFM tip driven by an antenna effect. The confined fields are tightly attached to the tip surface (evanescent fields) and produce an IR probe with dimensions comparable to the tip radius (no longer diffraction-limited after tip confinement) (*21*). When near the sample's surface (Fig. 1), the s-SNOM probe produces a scattered wave that carries the nanoscale-resolved dielectric response of the material. Demodulation at higher harmonics of the AFM tip dynamics and asymmetric interferometric detection allow s-SNOM to measure the amplitude and phase of the tip scattered wave and, hence, allow a background-free reconstruction of the complex optical response of the material (*22*). Ultimately, s-SNOM has reached unprecedented molecular sensitivity with its combination with broadband lasers (*23*, *24*), laser-driven plasma (*25*), and synchrotron IR nanospectroscopy (nano-FTIR) (*26*–*29*). Applied to a variety of multidisciplinary studies (*30*–*34*), nano-FTIR is a spectral imaging modality able to simultaneously reconstruct AFM topography and broadband IR response of the sample surface with nanoscale spatial resolution (Fig. 1). On the basis of the morphology and IR broadband intensity contrast from the nano-FTIR images, full IR spectral analysis can be performed at locations of interest.

We report herein, through synchrotron nano-FTIR, local heterogeneities in vibrational activity in fresh and degraded lead-based OIHP films. Despite the narrow morphological dispersion of the grained film, specific grains feature stronger vibrational activity, associated to degraded grains (PbI_2), in clear contrast to the homogeneous overall response. It was possible to distinguish and locate nanograins formed by hexagonal polytypes (nonperovskite yellow phases) within a rich background of cubic, black phase perovskite.

RESULTS

In nano-FTIR, both AFM topography and broadband IR s-SNOM response can be acquired simultaneously. Figure 2 (A and B) displays a 5 μm by 5 μm AFM topography and IR broadband intensity

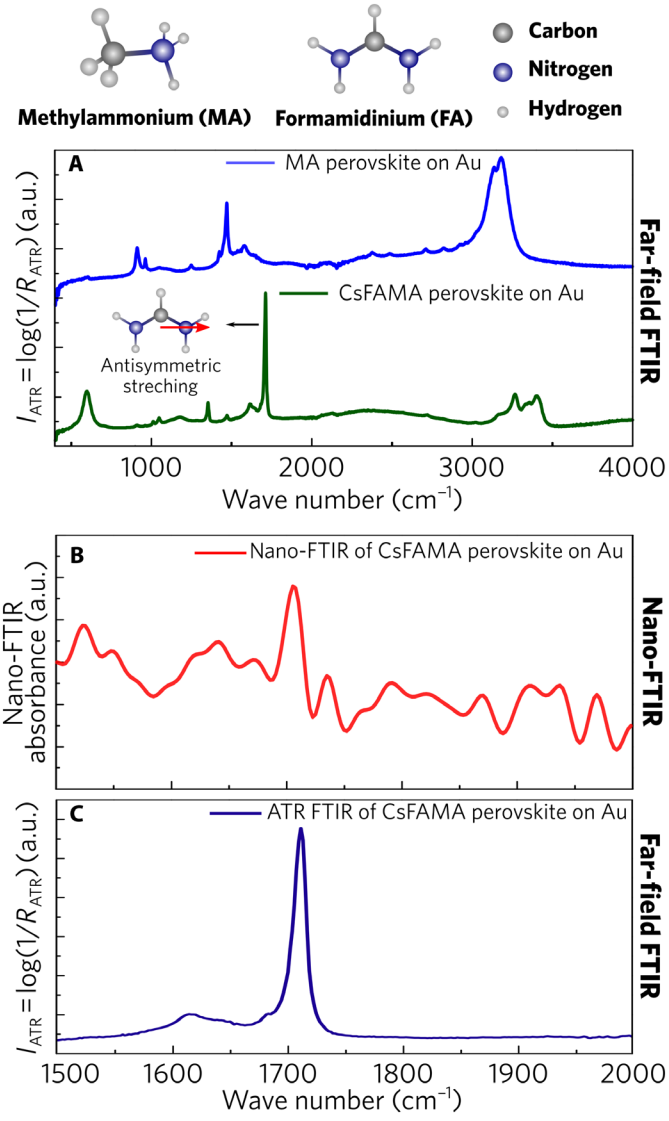

Fig. 3. ATR-FTIR and nano-FTIR comparison of perovskites. (**A**) Far-field ATR-FTIR absorbance of $MAPbI_3$ (top) and CsFAMA (bottom) perovskite films. The main molecular absorption of MA at 1470 cm^{-1} (symmetric NH_3^+ stretching) is very low in CsFAMA perovskite related to the molecular ratio between MA and FA. In the CsFAMA spectrum, the main molecular absorption around 1700 cm^{-1} is attributed to antisymmetric C-N stretching of the FA molecule. Nano-FTIR absorbance spectrum (**B**) and respective ATR-FTIR far-field spectrum (**C**) of a 370-nm-thick CsFAMA perovskite film. a.u., arbitrary units.

maps of a CsFAMA [$Cs_{0.05}FA_{0.79}MA_{0.16}Pb(I_{0.83}Br_{0.17})_3$] (*4*) pristine perovskite film. A solar cell based on this composition achieves efficiency higher than 20% (fig. S1). In the topography map in Fig. 2A, we identify a rather uniform distribution of grains with dimensions ranging from 200 to 400 nm forming a cohesive background film. Few isolated grains, with similar dimensions, excel in height and present a morphological contrast on top of the even background layer. The thickness of the CsFAMA perovskite film was measured as 372 ± 31 nm, which is comparable to the lateral dimensions of the grains. Thus, we can conclude that the film is composed of a monolayer of perovskite grains, as shown by a high-resolution cross-sectional scanning electron microscopy (SEM) image of the device (fig. S2), decorated with isolated grains atop. In the respective IR broadband map (Fig. 2B), most of the isolated grains present stronger s-SNOM scattering intensity responses compared to the background layer [inset a in Fig. 2 (A and B)]. However, few grains do not correlate IR response and AFM topography, as one can notice by comparing inset b in Fig. 2 (A and B).

Figure 2 (D and E) presents AFM topography and IR broadband map for an intentionally degraded CsFAMA perovskite film. Average grain size increased (300 to 800 nm) with a similar trend for the roughness (Ra) that evolved from 16.31 (before degradation) to 27.42 nm after degradation. As expected, sample degradation increased the vibrational activity of the even background layer as can be seen in the IR broadband intensity histograms in Fig. 2 (C and F). In the histograms, each pixel in the 200 × 200 pixel maps was binned according to its vibrational activity value. The maximum intensity shifted from 0.36 to 0.48 with broader distribution in the degraded sample.

Far-field absorption spectra of the $MAPbI_3$ and CsFAMA samples measured by attenuated total reflection FTIR (ATR-FTIR) are presented in Fig. 3A. ATR-FTIR of the MA perovskite film (Fig. 3A, top curve) features vibrational modes at 3180 cm^{-1} (N-H stretch), 3138 cm^{-1} (N-H stretch), 1574 cm^{-1} (antisymmetric NH_3^+ bend), 1470 cm^{-1} (symmetric NH_3^+ bend), 963 cm^{-1} (C-N stretch), and 911 cm^{-1} (NH_3^+/CH_3 rock) (*35*, *36*). In comparison, the CsFAMA perovskite film ATR-FTIR analysis (Fig. 3A, bottom curve) presents new vibrational resonances owing to the formamidinium (FA) cation at 3406 cm^{-1} (N-H stretch), 3357 cm^{-1} (N-H stretch), 3271 cm^{-1} (N-H stretch), 3167 cm^{-1} (N-H stretch), and 1714 cm^{-1} (C-N antisymmetric stretching) (*37*, *38*). In the CsFAMA sample, an additional weak line at 1472 cm^{-1} corresponds to the MA cation found in a smaller molar ratio in relation to FA (17% mol of MA in relation to FA). Figure 3 (B and C) shows nano-FTIR and ATR-FTIR absorbance spectra of the same CsFAMA perovskite film to compare the two techniques. Both spectra present similar vibrational features with a strong absorption at 1712 cm^{-1} that corresponds to antisymmetric C-N stretching of the FA cation molecule. The main absorption line of MA was not observed in the nano-FTIR spectrum because of the smaller amount of this cation molecule in the CsFAMA perovskite films. Our spectral analysis was restricted to the range covered by the nano-FTIR (3000 to 700 cm^{-1}) and, hence, only approaches FA components at the A site of the perovskite material.

To further understand the measured heterogeneities in both morphology and IR broadband maps, we selected regions of interest with different contrasts for detailed investigation of the chemical composition via nano-FTIR point spectra. Figure 4 (A and B) presents a 1 μm by 1 μm CsFAMA AFM topography and IR broadband images, respectively. Figure 4A shows a smooth surface topography with isolated grains that are few hundreds of nanometers wide. In contrast, the IR broadband image shows heterogeneity in vibrational activity, which is not completely associated with topography, as shown by the profiles in Fig. 4C. For the chemical composition investigation, nano-FTIR spectra were taken at points marked by numbers in Fig. 4 (A and B). The spectra were taken in two distinct regions according to their stronger or weaker vibrational response. To ensure reliability in both regions, three different points of each were chosen for the point nano-FTIR analysis. The spectra collected in the regions with homogeneous IR broadband response (points 1 to 3 in Fig. 4D) present the FA characteristic vibrational mode at

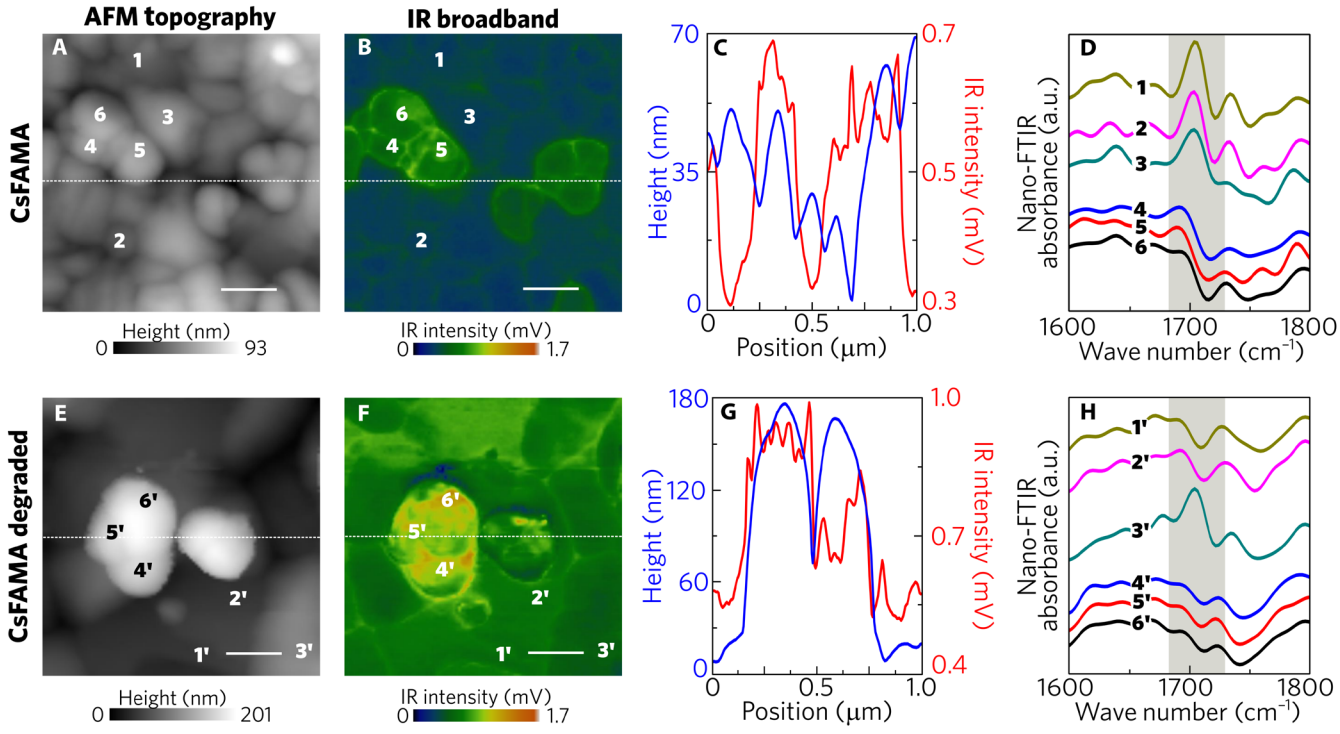

Fig. 4. Nanoscale chemical composition investigation by nano-FTIR. (**A** and **E**) AFM topography map (1 μm by 1 μm) of pristine CsFAMA and degraded CsFAMA perovskites, respectively. (**B** and **F**) Respective IR broadband images revealing heterogeneity in vibrational activity. Topography and IR broadband response do not completely correlate, as shown by the profiles in (**C**) and (**G**) related to pristine and degraded CsFAMA, respectively. (**D** and **H**) Nano-FTIR point spectra from the regions marked by numbers in (A), (B), (E), and (F). The characteristic vibrational mode of FA shows up only in grains with a weaker IR broadband response. For the degraded CsFAMA (H), the FA vibrational mode is less pronounced. The location 3′ is one of the few where the FA mode can be seen outside isolated grains. Scale bars, 200 nm.

1710 cm^{-1}, suggesting the presence of this cation molecule in these regions. However, in the regions with stronger IR activity (points 4 to 6), the FA vibrational mode is absent in the spectra, therefore revealing grains with poor concentration of FA molecular cations.

Further supported by XRD data, we preliminarily interpret here that regions with undetectable FA vibrational mode could be majorly composed of lead iodide (PbI_2), which is an alternative phase typically found in these perovskites. To verify this hypothesis, we intentionally degraded the CsFAMA film by heating it on a hot plate under air environment to increase the amount of the PbI_2 (*39*). As recently reported by Tan *et al.* (*39*), the CsFAMA degradation occurs in two stages when induced by heating: A loss of MA takes place at lower temperatures, followed by a loss of FA resulting in the formation of PbI_2. The annealing procedure was carried out in steps during the nano-FTIR sessions at the Brazilian Synchrotron Light Laboratory (LNLS). In a first step, the sample was heated at 100°C for 30 min. The morphology and broadband IR response were not substantial changed by the initial degrading procedure. However, the vibrational activity increased at the grain boundaries (see fig. S3). The CsFAMA sample contains 16% of MA, and we attribute the stronger vibrational activity at grain boundaries to the formation of PbI_2 due to MA loss. Then, a second heating step at 130°C for 2.5 hours was carried out. As shown in Fig. 2 (D and F), the vibrational activity of degraded CsFAMA is stronger in relation to the pristine film, with a similar trend, in the perspective of isolated grains (Fig. 4, E and F), however, with enhanced contrast. The same trend, with enhanced contrast, is observed in the perspective of isolated grains (Fig. 4, E and F). The profiles of the degraded CsFAMA sample (Fig. 4G) resembles the fresh sample, where particles with higher height are not necessarily related to stronger IR intensities. The even background layer, which was originally weaker and presented FA lines (Fig. 4, B and D), is now stronger, i.e., presents stronger IR activity, and does not show the characteristic FA absorption line. This is confirmed by the spectra (Fig. 4H) collected at points 4′ to 6′. Point spectra were also taken in the background layer (points 1′ to 3′) where this absorption was absent. Point 3′ (Fig. 4F) presents the absorption assigned to the FA cation, consistent with the fact that this region has weaker IR activity. We can preliminarily conclude that FA loss is not complete and that the degraded CsFAMA sample is mainly composed of a material either without or with low concentration of FA molecules. We assume the former to be PbI_2.

To confirm the composition of the pristine and degraded CsFAMA, we carried out high-resolution XRD at the XRD2 beamline of the LNLS. The measurements were performed at 7 keV. The XRD data shown in Fig. 5 (A and B) support the interpretations from the nano-FTIR analysis. The fresh CsFAMA sample exhibits the diffraction pattern of the cubic perovskite with the presence of PbI_2 and a minor peak of the hexagonal polytype 4H (*40*). By Rietveld analysis, we estimated that this sample was composed of a mass fraction of 0.01(1) of PbI_2 and 0.98(2) of perovskite (see table S1). The intentional degradation of CsFAMA converted part of the perovskite into PbI_2, observed by the increase in the intensity of the diffraction peak attributed to this phase (Fig. 5B) (see also fig. S4). The diffraction peaks from the cubic perovskite are still present but with smaller intensity, indicating incomplete induced degradation by heating. The mass fractions were estimated to be 0.48(8) of PbI_2 and 0.52(8)

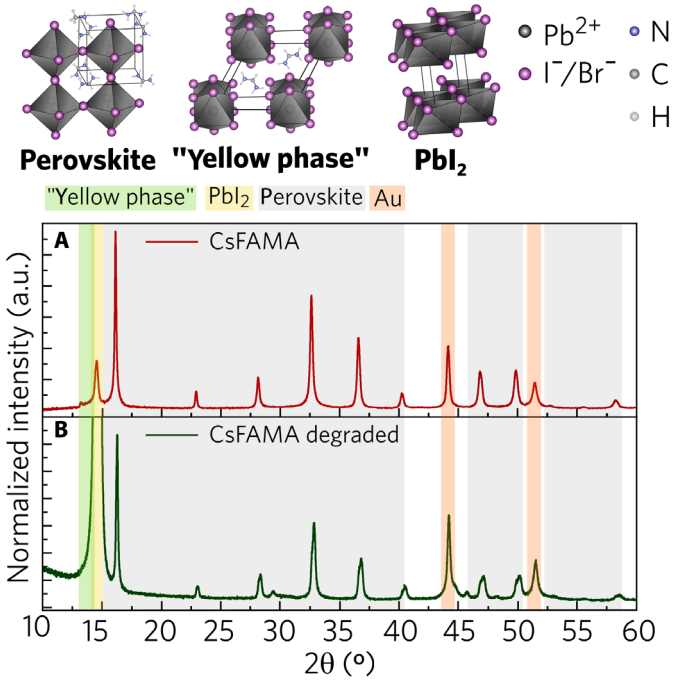

Fig. 5. Structural characterization through high-resolution XRD. Crystal structure of black perovskite (α-phase) with a cubic structure (*Pm*3*m* space group), yellow $FAPbI_3$ nonperovskite (δ-phase or 2H polytype) with a hexagonal structure (*P*63*mc* space group), and lead iodide (PbI_2) with a hexagonal structure (*Pm*1 space group). The high-resolution diffractogram (**A**) of the CsFAMA sample confirms the α-phase perovskite and lead iodide in smaller quantity. The intensity of the PbI_2 diffraction peak (**B**) of the CsFAMA degraded sample increased. The complete XRD of the CsFAMA degraded sample is available in the Supplementary Materials (fig. S4). The high-resolution XRD measurements were performed at 7 keV.

of perovskite. This result corroborates with nano-FTIR, in which the FA absorption is absent in most regions of the sample and the vibrational activity is stronger. Regions of stronger activity are associated to the more metallic character of PbI_2 compared to the perovskite.

We also investigated FA MA perovskite films [$FA_{0.83}MA_{0.17}Pb(I_{0.83}Br_{0.17})_3$ (FAMA)]. The FAMA sample was prepared in the same manner as the previous ones, but it does not contain cesium in the structure. It is well established that the incorporation of Cs is important to suppress the formation of nonperovskite yellow phase [δ-phase or 2H (*40*)]. The AFM topography and the IR broadband images, shown in Fig. 6 (A and C) and Fig. 6 (B and D) within areas of 5 μm by 5 μm and 1 μm by 1 μm, respectively, present similar features compared to CsFAMA. A background layer was decorated with isolated grains atop. The profiles in Fig. 6E also show that morphology and vibrational activity are not completely associated. However, the absorption from FA molecular cation at 1710 cm^{-1} is found in all locations marked (curves 1″ to 6″ in Fig. 6F). These observations are different from those found in the fresh CsFAMA samples where the vibrational mode of FA was absent in the isolated grains. A detailed nano-FTIR spectral analysis from a variety of locations in a specific area of the FAMA film can be found in fig. S5. We observed that the spectra collected at stronger IR activity regions [locations 4″ to 6″ in Fig. 6 (C and D)] presented less intense FA absorption in comparison to the dots in the weaker IR background layer [locations 1″ to 3″ in Fig. 6 (C and D)]. The diffractogram of the FAMA sample (Fig. 6G) confirms not only the cubic perovskite formation but also the presence of diffraction peaks related to hexagonal polytypes (2H, 4H, and 6H) and PbI_2. We estimated that the FAMA sample is composed of 0.78(5) of perovskite mass fraction and 0.22(5) of hexagonal polytypes.

The absorption coefficient of the coexistent phases is different and varies according to composition and structure. According to IR activity and XRD analysis of the FAMA sample, we can classify the nanograins into two distinct groups: nanograins with smaller and higher FA absorption. The isolated nanograins with smaller FA nano-FTIR absorbance [points 4″ to 6″ in Fig. 6 (C and D)] are those with a hexagonal shape. We interpret these hexagonal nanograins as formed by hexagonal polytypes (nonperovskite yellow phases). The even background layer with stronger FA absorption is composed, in its majority, of cubic, black phase perovskite.

CONCLUSIONS

We chemically mapped different coexisting nanoscale phases in OIHP using nano-FTIR, complemented by XRD. Our work focuses on both broadband imaging and nanoscale spectral analysis across IR fingerprints with 25-nm resolution, unveiling unprecedented chemical information on the grain-by-grain scale. Nano-FTIR broadband maps express local scattering properties of the material, which is proportional to the complex dielectric response.

CsFAMA perovskite films presented a heterogeneity in the nano-FTIR vibrational activity, in both pristine and degraded states, where regions with stronger vibrational response are depleted of the FA cation molecule. These regions have a larger effective polarizability and have been assigned to the presence of the PbI_2 phase compound. The combination of broadband maps and nanoscale spectra shows clear evidence that FA depletion, i.e., early degradation stages, takes place in a grain-by-grain scale. In the FAMA perovskite films, which were also heterogeneous, it was possible to distinguish and locate nanograins with hexagonal shapes formed by hexagonal polytypes (nonperovskite yellow phases) in a homogeneous film layer richer in cubic, black phase perovskite. These hexagonal polytypes also showed larger effective polarizability compared to the black perovskite phase. Our work reveals that nano-FTIR provides a unique tool for tracking morphological and chemical properties of isolated perovskite nanograins. Mixed cation multiple halide perovskites are excellent materials to be explored by this technique since it is expected that the distribution of the different phases does not happen uniformly and may evolve after exposure to different external factors such as light, temperature, and moisture. The approach used here can be extended to other perovskite studies where the connection between local morphology and chemistry can potentially affect the device performance.

MATERIALS AND METHODS

Sample preparation

The perovskite film used in this work was CsFAMA, which can achieve efficiency above 20% in solar cells (*1*). Perovskite films were prepared inside a glove box filled with nitrogen by solvent engineering method using a mixture of dimethyl sulfoxide and dimethylformamide (1:4 v/v) and chlorobenzene as antisolvent. This method presents the best results to prepare highly efficient PSCs. One sample of CsFAMA was intentionally degraded by heating in a hot plate under air. Details of preparation are available in the Supplementary Materials.

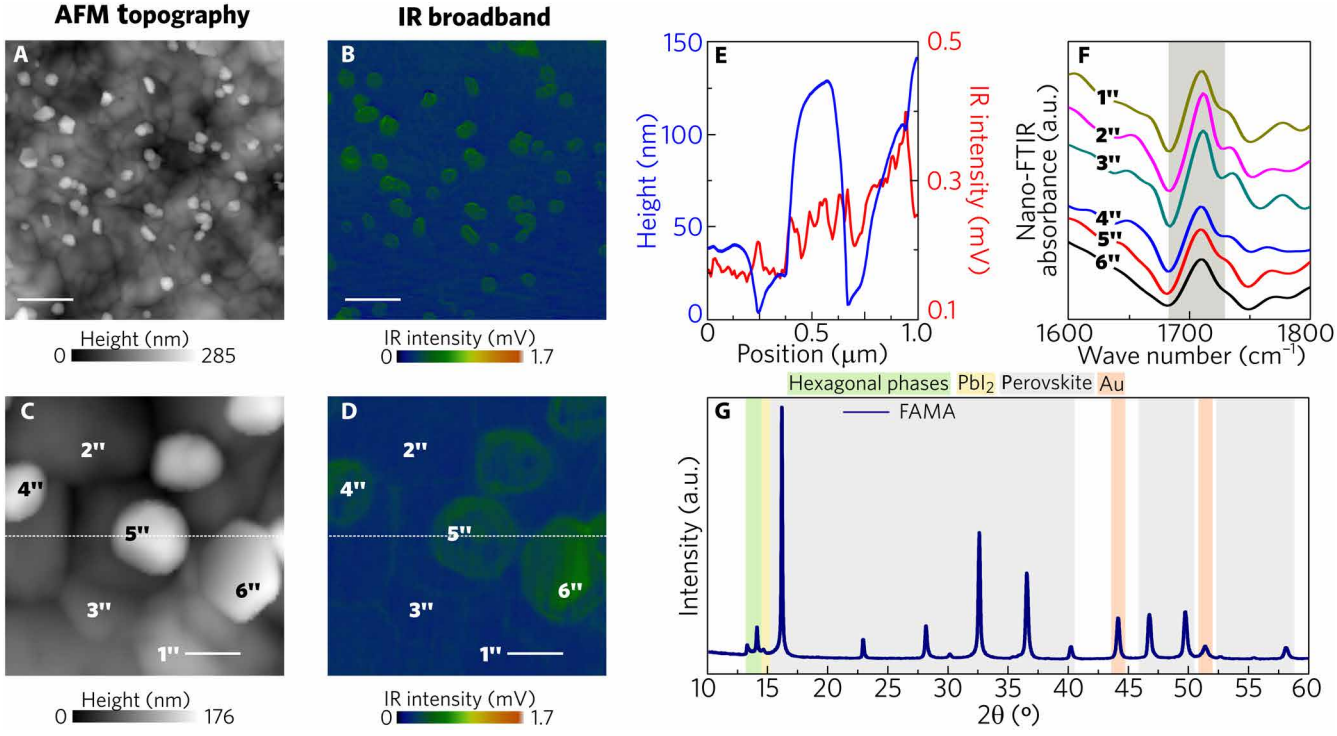

Fig. 6. Nanoscale chemical composition investigation by nano-FTIR of FAMA perovskite. (**A** and **B**) AFM topography map (5 μm by 5 μm) of FAMA perovskite and IR broadband image, respectively (scale bars, 200 nm). (**C** and **D**) Respective 1 μm by 1 μm images revealing heterogeneity in vibrational activity similar to pristine CsFAMA perovskite (scale bars, 200 nm). (**E**) Profiles of the topography and IR broadband. (**F**) Nano-FTIR point spectra from the regions marked in (C) and (D) reveal the presence of vibrational mode of FA in all marked locations. (**G**) The XRD pattern reveals that the FAMA sample is composed mostly of cubic perovskite, hexagonal phases, and PbI_2 in less quantity. The high-resolution XRD measurements were performed at 7 keV.

Nano-FTIR experiment

Nano-FTIR experiments were carried out at the LNLS in the IR1 beamline (*29*). Ultrabroadband IR radiation (THz to visible) extracted from a 1.67-T bending magnet in the 1.37-GeV storage ring was focused and collimated by low-aberration optics and then propagated up to a commercial s-SNOM instrument (NeaSNOM; Neaspec GmbH) in the IR1 experimental station (*29*). The AFM was operated in ~250-kHz tapping mode with metallic tips (Arrow PtIr; NanoWorld AG), and s-SNOM detection was performed using a mercury cadmium telluride (MCT) detector (50 μm by 50 μm chip area; InfraRed Associates Inc.). All IR broadband images were normalized by the storage ring current and were acquired with blocked interferometer arm (self-homodyne detection); hence, every pixel corresponds to an integral of the s-SNOM amplitude response across the MCT detector frequency range. Point spectra were acquired with 10 cm^{-1} spectral resolution, 2048 points per interferogram, and 20-ms integration time per point. All point spectra are an average of 30 Fourier-processed interferograms. It is important to state that all IR broadband maps presented are amplitude intensity; therefore, they express local scattering properties of the material. All experiments were performed under a N_2-purged environment with relative humidity <2%. All data presented were intensity-corrected by the storage ring current decay and then normalized by a reference spectrum acquired from a clean Au surface to subtract the environment and detector functions.

Far-field FTIR and XRD characterization

Far-field FTIR spectroscopy was collected using the spectrophotometer Agilent model Cary 630 FTIR in ATR geometry using a diamond crystal. The synchrotron radiation XRD was performed at the XRD2 beamline of the LNLS using an energy of 7 keV (λ = 1.7712 Å) in 10° < 2θ < 60°. The detector was a MYTHEN 1K from DECTRIS, mounted on grazing-incidence diffraction. The incidence angle was 4°, and the measurements were performed at room temperature. Materials and Methods should provide sufficient information to allow replication of the results. Begin with a section titled Experimental Design describing the objectives and design of the study as well as prespecified components.

SUPPLEMENTARY MATERIALS

Supplementary material for this article is available at http://advances.sciencemag.org/cgi/content/full/5/10/eaaw6619/DC1

Perovskite preparation

Solar cell characterization

Fig. S1. Photovoltaic performance of CsFAMA solar cell.

Fig. S2. High-resolution cross-sectional SEM image of the device.

Fig. S3. Nano-FTIR of the intentionally degraded CsFAMA film at 100°C for 30 min.

Fig. S4. High-resolution XRD pattern of the CsFAMA degraded perovskite sample deposited onto Si/Au substrate.

Fig. S5. Comparison between intensity of the spectra collected at different regions of the FAMA film.

Table S1. Film composition as obtained from Rietveld refinement using the software MAUD.

REFERENCES AND NOTES

1. D. Bi, W. Tress, M. I. Dar, P. Gao, J. Luo, C. Renevier, K. Schenk, A. Abate, F. Giordano, J.-P. C. Baena, J.-D. Decoppet, S. M. Zakeeruddin, M. K. Nazeeruddin, M. Grätzel, A. Hagfeldt, Efficient luminescent solar cells based on tailored mixed-cation perovskites. *Sci. Adv.* **2**, e1501170 (2016).
2. J. M. Frost, K. T. Butler, F. Brivio, C. H. Hendon, M. van Schilfgaarde, A. Walsh, Atomistic origins of high-performance in hybrid halide perovskite solar cells. *Nano Lett.* **14**, 2584–2590 (2014).

3. M. Li, C. Zhao, Z.-K. Wang, C.-C. Zhang, H. K. H. Lee, A. Pockett, J. Barbé, W. C. Tsoi, Y.-G. Yang, M. J. Carnie, X.-Y. Gao, W.-X. Yang, J. R. Durrant, L.-S. Liao, S. M. Jain, Interface modification by ionic liquid: A promising candidate for indoor light harvesting and stability improvement of planar perovskite solar cells. *Adv. Energy Mater.* **8**, 1801509 (2018).
4. M. Saliba, T. Matsui, J.-Y. Seo, K. Domanski, J.-P. Correa-Baena, M. K. Nazeeruddin, S. M. Zakeeruddin, W. Tress, A. Abate, A. Hagfeldt, M. Grätzel, Cesium-containing triple cation perovskite solar cells: Improved stability, reproducibility and high efficiency. *Energy Environ. Sci.* **9**, 1989–1997 (2016).
5. M. Saliba, T. Matsui, K. Domanski, J.-Y. Seo, A. Ummadisingu, S. M. Zakeeruddin, J.-P. Correa-Baena, W. R. Tress, A. Abate, A. Hagfeldt, M. Grätzel, Incorporation of rubidium cations into perovskite solar cells improves photovoltaic performance. *Science* **354**, 206–209 (2016).
6. S. Cacovich, G. Divitini, C. Ireland, F. Matteocci, A. D. Carlo, C. Ducati, Elemental mapping of perovskite solar cells by using multivariate analysis: An insight into degradation processes. *ChemSusChem* **9**, 2673–2678 (2016).
7. J. A. Christians, P. Schulz, J. S. Tinkham, T. H. Schloemer, S. P. Harvey, B. J. T. de Villers, A. Sellinger, J. J. Berry, J. M. Luther, Tailored interfaces of unencapsulated perovskite solar cells for >1,000 hour operational stability. *Nat. Energy* **3**, 68–74 (2018).
8. P. Gratia, G. Grancini, J.-N. Audinot, X. Jeanbourquin, E. Mosconi, I. Zimmermann, D. Dowsett, Y. Lee, M. Grätzel, F. De Angelis, K. Sivula, T. Wirtz, M. K. Nazeeruddin, Intrinsic halide segregation at nanometer scale determines the high efficiency of mixed cation/mixed halide perovskite solar cells. *J. Am. Chem. Soc.* **138**, 15821–15824 (2016).
9. V. Kumar, W. L. Schmidt, G. Schileo, R. C. Masters, M. Wong-Stringer, D. C. Sinclair, I. M. Reaney, D. Lidzey, C. Rodenburg, Nanoscale mapping of bromide segregation on the cross sections of complex hybrid perovskite photovoltaic films using secondary electron hyperspectral imaging in a scanning electron microscope. *ACS Omega* **2**, 2126–2133 (2017).
10. S. Lilliu, T. G. Dane, M. Alsari, J. Griffin, A. T. Barrows, M. S. Dahlem, R. H. Friend, D. G. Lidzey, J. E. Macdonald, Mapping morphological and structural properties of lead halide perovskites by scanning nanofocus XRD. *Adv. Funct. Mater.* **26**, 8221–8230 (2016).
11. J.-P. Correa-Baena, Y. Luo, T. M. Brenner, J. Snaider, S. Sun, X. Li, M. A. Jensen, N. T. P. Hartono, L. Nienhaus, S. Wieghold, J. R. Poindexter, S. Wang, Y. S. Meng, T. Wang, B. Lai, M. V. Holt, Z. Cai, M. G. Bawendi, L. Huang, T. Buonassisi, D. P. Fenning, Homogenized halides and alkali cation segregation in alloyed organic-inorganic perovskites. *Science* **363**, 627–631 (2019).
12. A. Dazzi, R. Prazeres, F. Glotin, J. M. Ortega, Local infrared microspectroscopy with subwavelength spatial resolution with an atomic force microscope tip used as a photothermal sensor. *Opt. Lett.* **30**, 2388–2390 (2005).
13. L. Wang, H. Wang, M. Wagner, Y. Yan, D. S. Jakob, X. G. Xu, Nanoscale simultaneous chemical and mechanical imaging via peak force infrared microscopy. *Sci. Adv.* **3**, e1700255 (2017).
14. D. Nowak, W. Morrison, H. K. Wickramasinghe, J. Jahng, E. Potma, L. Wan, R. Ruiz, T. R. Albrecht, K. Schmidt, J. Frommer, D. P. Sanders, S. Park, Nanoscale chemical imaging by photoinduced force microscopy. *Sci. Adv.* **2**, e1501571 (2016).
15. Y. Yuan, J. Chae, Y. Shao, Q. Wang, Z. Xiao, A. Centrone, J. Huang, Photovoltaic switching mechanism in lateral structure hybrid perovskite solar cells. *Adv. Energy Mater.* **5**, 1500615 (2015).
16. R. Dong, Y. Fang, J. Chae, J. Dai, Z. Xiao, Q. Dong, Y. Yuan, A. Centrone, X. C. Zeng, J. Huang, High-gain and low-driving-voltage photodetectors based on organolead triiodide perovskites. *Adv. Mater.* **27**, 1912–1918 (2015).
17. J. Chae, Q. Dong, J. Huang, A. Centrone, Chloride incorporation process in $CH_3NH_3PbI_{3-x}Cl_x$ perovskites via nanoscale bandgap maps. *Nano Lett.* **15**, 8114–8121 (2015).
18. E. Strelcov, Q. Dong, T. Li, J. Chae, Y. Shao, Y. Deng, A. Gruverman, J. Huang, A. Centrone, $CH_3NH_3PbI_3$ perovskites: Ferroelasticity revealed. *Sci. Adv.* **3**, e1602165 (2017).
19. B. Knoll, F. Keilmann, Near-field probing of vibrational absorption for chemical microscopy. *Nature* **399**, 134–137 (1999).
20. F. Zenhausern, Y. Martin, H. K. Wickramasinghe, Scanning interferometric apertureless microscopy: Optical imaging at 10 angstrom resolution. *Science* **269**, 1083–1085 (1995).
21. F. Keilmann, R. Hillenbrand, Near-field microscopy by elastic light scattering from a tip. *Philos. Trans. A.* **362**, 787–805 (2004).
22. A. A. Govyadinov, I. Amenabar, F. Huth, P. Scott Carney, R. Hillenbrand, Quantitative measurement of local infrared absorption and dielectric function with tip-enhanced near-field microscopy. *J. Phys. Chem. Lett.* **4**, 1526–1531 (2013).
23. F. Huth, A. Govyadinov, S. Amarie, W. Nuansing, F. Keilmann, R. Hillenbrand, Nano-FTIR absorption spectroscopy of molecular fingerprints at 20 nm spatial resolution. *Nano Lett.* **12**, 3973–3978 (2012).
24. I. Amenabar, S. Poly, M. Goikoetxea, W. Nuansing, P. Lasch, R. Hillenbrand, Hyperspectral infrared nanoimaging of organic samples based on Fourier transform infrared nanospectroscopy. 8, 14402 (2017).
25. M. Wagner, D. S. Jakob, S. Horne, H. Mittel, S. Osechinskiy, C. Phillips, G. C. Walker, C. Su, X. G. Xu, Ultra-broadband nano-spectroscopy with a laser-driven plasma sources. *ACS Photonics* **5**, 1467–1475 (2018).
26. P. Hermann, A. Hoehl, P. Patoka, F. Huth, E. Rühl, G. Ulm, Near-field imaging and nano-Fourier-transform infrared spectroscopy using broadband synchrotron radiation. *Opt. Express* **21**, 2913–2919 (2013).
27. H. A. Bechtel, E. A. Muller, R. L. Olmon, M. C. Martin, M. B. Raschke, Ultrabroadband infrared nanospectroscopic imaging. *Proc. Natl. Acad. Sci. U.S.A.* **111**, 7191–7196 (2014).
28. B. Pollard, F. C. B. Maia, M. B. Raschke, R. O. Freitas, Infrared vibrational nanospectroscopy by self-referenced interferometry. *Nano Lett.* **16**, 55–61 (2016).
29. R. O. Freitas, C. Deneke, F. C. B. Maia, H. G. Medeiros, T. Moreno, P. Dumas, Y. Petroff, H. Westfahl, Low-aberration beamline optics for synchrotron infrared nanospectroscopy. *Opt. Express* **26**, 11238–11249 (2018).
30. I. Amenabar, S. Poly, W. Nuansing, E. H. Hubrich, A. A. Govyadinov, F. Huth, R. Krutokhvostov, L. Zhang, M. Knez, J. Heberle, A. M. Bittner, R. Hillenbrand, Structural analysis and mapping of individual protein complexes by infrared nanospectroscopy. *Nat. Commun.* **4**, 2890 (2013).
31. I. Barcelos, A. R. Cadore, L. C. Campos, A. Malachias, K. Watanabe, T. Taniguchi, F. C. B. Maia, R. Freitas, C. Deneke, Graphene/h-BN plasmon-phonon coupling and plasmon delocalization observed by infrared nano-spectroscopy. *Nanoscale* **7**, 11620–11625 (2015).
32. Z. Shi, H. A. Bechtel, S. Berweger, Y. Sun, B. Zeng, C. Jin, H. Chang, M. C. Martin, M. B. Raschke, F. Wang, Amplitude- and phase-resolved nanospectral imaging of phonon polaritons in hexagonal boron nitride. *ACS Photonics* **2**, 790–796 (2015).
33. C.-Y. Wu, W. J. Wolf, Y. Levartovsky, H. A. Bechtel, M. C. Martin, F. D. Toste, E. Gross, High-spatial-resolution mapping of catalytic reactions on single particles. *Nature* **541**, 511–515 (2017).
34. E. A. Muller, B. Pollard, H. A. Bechtel, P. van Blerkom, M. B. Raschke, Infrared vibrational nanocrystallography and nanoimaging. *Sci. Adv.* **2**, e1601006 (2016).
35. J. B. Patel, R. L. Milot, A. D. Wright, L. M. Herz, M. B. Johnston, Formation dynamics of $CH_3NH_3PbI_3$ perovskite following two-step layer deposition. *J. Phys. Chem. Lett.* **7**, 96–102 (2016).
36. M. A. Pérez-Osorio, R. L. Milot, M. R. Filip, J. B. Patel, L. M. Herz, M. B. Johnston, F. Giustino, Vibrational properties of the organic–inorganic halide perovskite $CH_3NH_3PbI_3$ from theory and experiment: Factor group analysis, first-principles calculations, and low-temperature infrared spectra. *J. Phys. Chem. C* **119**, 25703–25718 (2015).
37. K. Hills-Kimball, Y. Nagaoka, C. Cao, E. Chaykovsky, O. Chen, Synthesis of formamidinium lead halide perovskite nanocrystals through solid–liquid–solid cation exchange. *J. Mater. Chem. C* **5**, 5680–5684 (2017).
38. V. C. A. Taylor, D. Tiwari, M. Duchi, P. M. Donaldson, I. P. Clark, D. J. Fermin, T. A. A. Oliver, Investigating the role of the organic cation in formamidinium lead iodide perovskite using ultrafast spectroscopy. *J. Phys. Chem. Lett.* **9**, 895–901 (2018).
39. W. Tan, A. R. Bowring, A. C. Meng, M. D. McGehee, P. C. McIntyre, Thermal stability of mixed cation metal halide perovskites in air. *ACS Appl. Mater. Interfaces* **10**, 5485–5491 (2018).
40. P. Gratia, I. Zimmermann, P. Schouwink, J.-H. Yum, J.-N. Audinot, K. Sivula, T. Wirtz, M. K. Nazeeruddin, The many faces of mixed ion perovskites: Unraveling and understanding the crystallization process. *ACS Energy Lett.* **2**, 2686–2693 (2017).

Acknowledgments: We thank the LNLS for providing beamtime at beamlines IR1 and XRD2. **Funding:** R.S. thanks the São Paulo Research Foundation (FAPESP, grant 2017/12582-5). R.S. and A.F.N. acknowledge support from FAPESP (grant 2017/11986-5) and Shell and the strategic importance of the support given by ANP (Brazil's National Oil, Natural Gas and Biofuels Agency) through the R&D levy regulation. We also acknowledge the Swiss National Science Foundation for financial support with the project entitled "Fundamental studies of dye-sensitized and perovskite solar cells" with project number 200020_169695. **Author contributions:** R.S. and S.-H.T.-C. prepared the samples. R.S., J.C.S., H.C.N.T., and R.O.F. performed the nano-FTIR experiments. R.S. and M.M.S. performed the XRD measurements. R.S., M.M.S., R.O.F., A.H., H.C.N.T., and A.F.N. interpreted the results. R.S. wrote the manuscript with input from all authors. All the authors contributed to results discussion. **Competing interests:** The authors declare that they have no competing interests. **Data and materials availability:** All data needed to evaluate the conclusion in the paper are present in the paper and/or the Supplementary Materials. Additional data related to this paper may be requested from the authors.

Submitted 18 January 2019
Accepted 13 September 2019
Published 25 October 2019
10.1126/sciadv.aaw6619

Citation: R. Szostak, J. C. Silva, S.-H. Turren-Cruz, M. M. Soares, R. O. Freitas, A. Hagfeldt, H. C. N. Tolentino, A. F. Nogueira, Nanoscale mapping of chemical composition in organic-inorganic hybrid perovskite films. *Sci. Adv.* **5**, eaaw6619 (2019).

Nanoscale mapping of chemical composition in organic-inorganic hybrid perovskite films

R. Szostak, J. C. Silva, S.-H. Turren-Cruz, M. M. Soares, R. O. Freitas, A. Hagfeldt, H. C. N. Tolentino and A. F. Nogueira

Sci Adv **5** (10), eaaw6619.
DOI: 10.1126/sciadv.aaw6619